

# JGR Space Physics



## RESEARCH ARTICLE

10.1029/2021JA030227

### Key Points:

- MEX and MAVEN data are used to examine the response of Mars' induced magnetosphere to the solar wind
- We find that induced magnetic fields are enhanced relative to the IMF during intervals of lower dynamic pressure
- Comparing induced fields to the instantaneous IMF reveals more structure in the interaction region at high altitudes

### Correspondence to:

K. Stergiopoulou,  
[katerina@irfu.se](mailto:katerina@irfu.se)

### Citation:

Stergiopoulou, K., Andrews, D. J., Edberg, N. J. T., Halekas, J., Lester, M., Sánchez-Cano, B., et al. (2022). A two-spacecraft study of Mars' induced magnetosphere's response to upstream conditions. *Journal of Geophysical Research: Space Physics*, 127, e2021JA030227. <https://doi.org/10.1029/2021JA030227>

Received 17 DEC 2021  
Accepted 11 MAR 2022

## A Two-Spacecraft Study of Mars' Induced Magnetosphere's Response to Upstream Conditions

Katerina Stergiopoulou<sup>1,2</sup> , David J. Andrews<sup>1</sup> , Niklas J. T. Edberg<sup>1</sup> , Jasper Halekas<sup>3</sup> , Mark Lester<sup>4</sup> , Beatriz Sánchez-Cano<sup>4</sup>, Andrew P. Dimmock<sup>1</sup> , and Jacob R. Gruesbeck<sup>5</sup> 

<sup>1</sup>Swedish Institute of Space Physics, Uppsala, Sweden, <sup>2</sup>Space and Plasma Physics, Department of Physics and Astronomy, Uppsala University, Uppsala, Sweden, <sup>3</sup>Department of Physics and Astronomy, University of Iowa, Iowa City, IA, USA, <sup>4</sup>School of Physics and Astronomy, University of Leicester, Leicester, UK, <sup>5</sup>Goddard Space Flight Center, Greenbelt, MD, USA

**Abstract** This is a two-spacecraft study, in which we investigate the effects of the upstream solar wind conditions on the Martian induced magnetosphere and upper ionosphere. We use Mars Express (MEX) magnetic field magnitude data together with interplanetary magnetic field (IMF), solar wind density, and velocity measurements from the Mars Atmosphere and Volatile Evolution (MAVEN) mission, from November 2014 to November 2018. We compare simultaneous observations of the magnetic field magnitude in the induced magnetosphere of Mars ( $|B|_{IM}$ ) with the IMF magnitude ( $|B|_{IMF}$ ), and we examine variations in the ratio  $|B|_{IM}/|B|_{IMF}$  with solar wind dynamic pressure, speed and density. We find that the  $|B|_{IM}/|B|_{IMF}$  ratio in the induced magnetosphere generally decreases with increased dynamic pressure and that a more structured interaction is seen when comparing induced fields to the instantaneous IMF, where reductions in the relative fields at the magnetic pile up boundary (MPB) are more evident than in the field strength itself, along with enhancements in the immediate vicinity of the optical shadow of Mars. We interpret these results as evidence that while the induced magnetosphere is indeed compressed and induced field strengths are higher during periods of high dynamic pressure, a relatively larger amount of magnetic flux threads the region compared to that available from the unperturbed IMF during low dynamic pressure intervals.

**Plain Language Summary** The solar wind input to the Martian system plays a decisive role in formulating the morphology of the near-Mars plasma environment. Specifically, ion escape rates, the plasma boundary locations around the planet and the structure of the induced magnetosphere in general have been shown by numerous studies to be influenced by the upstream solar wind conditions. In this work, we use simultaneous measurements from MEX and MAVEN to probe the response of the Martian induced magnetosphere and upper ionosphere to different regimes of solar wind dynamic pressure, speed and density. We find that despite the stronger magnetic fields observed in the induced magnetosphere during periods of high solar wind dynamic pressure, when we compare these fields with the interplanetary magnetic field (IMF) measured simultaneously, we see in fact relative enhancements for low solar wind dynamic pressure.

## 1. Introduction

Mars has no intrinsic dipolar magnetic field with which to stand off the incoming solar wind. Instead its conducting ionosphere acts as an effective obstacle to the incoming solar wind and an induced magnetosphere is formed, the structure of which is determined for instance by the solar wind input, ultraviolet (UV) radiation, the Martian crustal magnetic fields and the underlying neutral atmosphere (Bertucci et al., 2011; Nagy et al., 2004). Many aspects of the Mars-solar wind interaction are outwardly comparable to those at Venus, as was extensively studied during the Pioneer-Venus era, and thus much of the understanding developed initially for Venus can be transferred to the Mars interaction, despite differences of scale, solar wind conditions, and so on (Luhmann & Cravens, 1991). Moreover, the Mars-solar wind interaction has been extensively studied in recent years by ESA's Mars Express (MEX) and NASA's Mars Atmosphere and Volatile Evolution (MAVEN) missions, and relevant aspects are summarized below.

The Mars-solar wind interaction is typically characterized by the formation of several distinct plasma boundaries separating regions of differing plasma properties and compositions. At the largest distances, the bow shock is formed upstream from the planet, inside which the solar wind is slowed, heated and deflected around the

© 2022 The Authors.

This is an open access article under the terms of the [Creative Commons Attribution-NonCommercial License](https://creativecommons.org/licenses/by/4.0/), which permits use, distribution and reproduction in any medium, provided the original work is properly cited and is not used for commercial purposes.

ionospheric obstacle in the magnetosheath (i.e., Hall et al., 2019; Mazelle et al., 2004; Vignes et al., 2000). The magnetic pile-up boundary (MPB, and sometimes alternately referred to as the induced magnetospheric boundary, IMB) is that surface that separates the heated solar wind plasma of the magnetosheath from the upper layers of the Martian ionosphere. Importantly, however, no strong consensus yet exists regarding the physical parameters that specifically delineate the MPB. It has variously been defined as a pressure-balance surface (Girazian et al., 2019; Holmberg et al., 2019), or by gradients in plasma and field pressures (Wang et al., 2021), and is also at least often well correlated with changes in the plasma composition from solar wind ( $H^+$ ) to planetary ions ( $O^+$ ,  $O_2^+$ ) dominated regimes (hence the occasionally used name, ion composition boundary, ICB; Halekas et al., 2018). Comparing these different definitions, it should be noted that the differences in location and behavior remain generally small compared to the intrinsic variability of the location of the MPB with upstream conditions. In this paper we adopt a definition of the MPB as the lower edge of the magnetosheath as being sufficient for the essentially illustrative purposes required here. Similarly, the magnetic pile up region (MPR) can be taken to be defined as the region below the MPB. A sharp gradient in plasma density, termed the ionopause, is also often observed at altitudes below the nominal MPB, and is named in analogy with a similar plasma boundary found in the unmagnetized state of the Venusian ionosphere and induced magnetosphere (e.g., Duru et al., 2009).

The locations of the bow shock as well as of the MPB have been determined and parameterized in several studies (i.e., Edberg et al., 2008; Gruesbeck et al., 2018; Němec et al., 2020; Trotignon et al., 2006; Vignes et al., 2000; Wang et al., 2020). These boundaries though are not fixed in altitude or shape, and appear to have a dynamic relationship with various parameters, such as extreme ultraviolet (EUV) radiation, crustal magnetic fields, solar wind parameters, interplanetary magnetic field (IMF) orientation, Martian seasons and solar cycle (Brain et al., 2005; Edberg et al., 2008, 2009; Hall et al., 2016, 2019; Matsunaga et al., 2017; Ramstad, Barabash, Futaana, & Holmström, 2017). The solar wind dynamic pressure ( $P_{dyn}$ ) has been examined as a controlling factor in the work of Crider et al. (2003), Brain et al. (2005), and Edberg et al. (2009). The solar wind dynamic pressure term dominates upstream of Mars, but in the magnetosheath, as the solar wind is decelerated and heated, the thermal pressure becomes significant compared to the dynamic pressure, while in the MPR the dominant term is the magnetic pressure (Crider et al., 2003; Dubinin et al., 2008; Holmberg et al., 2019). Crider et al. (2003), using the magnetic pressure in the MPR as a proxy for  $P_{dyn}$ , have shown that for high  $P_{dyn}$  the MPB moves closer to the planet. The dependence of the MPB location on  $P_{dyn}$  was additionally confirmed by Brain et al. (2005). The downward shifting of the bow shock and MPB locations during periods of high  $P_{dyn}$  was once more demonstrated in a statistical study by Edberg et al. (2009). The ionopause's location is also dependent on  $P_{dyn}$ , as when it is found (45% rate of occurrence in MAVEN electron density profiles) it is located at the altitude where the total ionospheric pressure approximately balances the solar wind dynamic pressure (Sánchez-Cano et al., 2020). Holmberg et al. (2019), following the earlier study by Dubinin et al. (2008) computed the individual contributions (dynamic, thermal, and magnetic) to the pressure in the plasma near the sub-solar point, showing clearly that a balance between the upstream dynamic pressure and the magnetic pressure in the induced magnetosphere is generally satisfied, though it may often not be appropriate to describe this region wholly by the complete separation of plasma regimes across well-defined boundaries.

Taking advantage of the long durations over which MEX and MAVEN have been orbiting Mars, the aim of this work is to further assess the response of the Martian induced magnetosphere to upstream conditions through simultaneous in-situ observations. In this paper, we combine data from MEX and MAVEN, taken during the period from November 2014 to November 2018, and compare the strength of the magnetic fields MEX measures in the induced magnetosphere with the upstream IMF as observed by MAVEN at the same time, for low, intermediate and high solar wind dynamic pressure, speed and density. This affords a comparison of the extent to which the induced magnetosphere is altered in its structure in response to variations in the solar wind, and provides a measure by which the draping of the IMF in the induced magnetosphere can be compared to the unperturbed solar wind. In Section 2 we present solar wind statistical correlations and results of the magnetospheric response to various upstream conditions, in Section 3 we discuss our findings and in Section 4 we summarize our main conclusions.

## 2. Observations

We use simultaneous measurements from the Mars Advanced Radar for Subsurface and Ionosphere Sounding (MARSIS) instrument on board MEX, and from the Solar Wind Ion Analyzer (SWIA) instrument and magnetometer (MAG) on board MAVEN during the period between November 2014 and November 2018, to observe

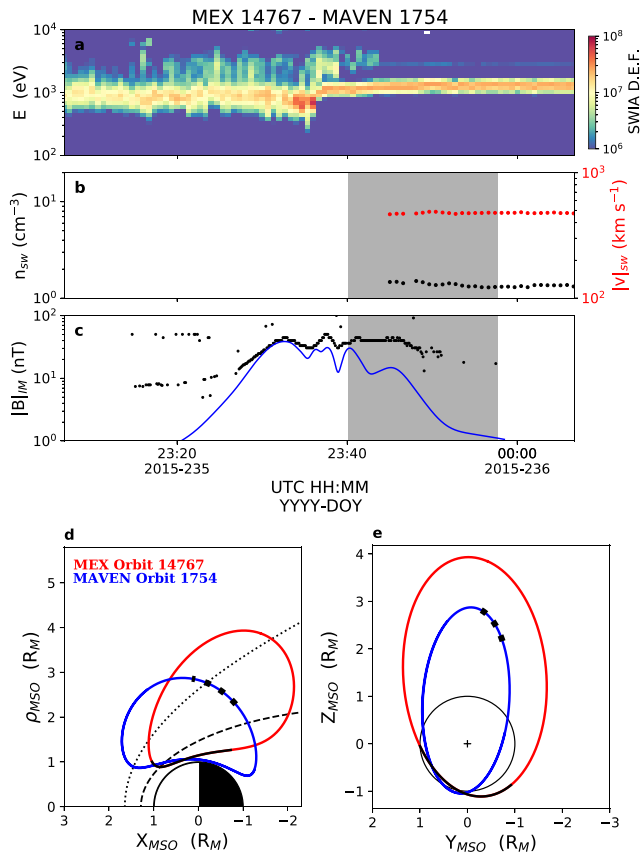


**Figure 1.** Example of simultaneous observations during MEX and MAVEN orbits 14767 and 1754 respectively, for parts of DOY 235 and 236. We show (a) the energy spectrum from SWIA with the differential energy flux (D.E.F.) color-coded in units of  $\text{eV}/(\text{cm}^2 \text{ s sr eV})$ , (b) the solar wind density (black circles, left axis) and speed (red circles, right axis) determined by SWIA (Halekas, Ruhunusiri, et al., 2017), (c) the magnetic field magnitude from MARSIS (Andrews et al., 2015) in black and the strength of the crustal magnetic fields at the spacecraft location in blue, based on the model by Cain et al. (2003), (d) the trajectories of the orbits of MEX in red and of MAVEN in blue in cylindrical MSO coordinates and (e) the trajectories of the orbits in the YZ MSO plane in Mars radii ( $R_M$ ) units. The gray shaded area in Figures 1b and 1c represents the simultaneous MEX and MAVEN data selected from these orbits. The dotted and dashed lines in Figure 1d denote the bow shock and MPB locations based on the model by Vignes et al. (2000), while the black part on the red MEX orbit and the black squares on MAVEN orbit, in Figures 1d and 1e, depict the interval MARSIS was operating in AIS mode and where MAVEN was located at that same interval, respectively.

the response of the induced magnetosphere of Mars to upstream solar wind conditions. The  $\sim 4$  years interval, from which the data used in this study comes from, is dictated primarily by the availability of extended measurements in the pristine solar wind by MAVEN. Due to the aerobraking phase that commenced in early 2019 and the subsequent reduction in apoapsis altitude, MAVEN now spends a smaller percentage of the time in the undisturbed solar wind.

When operated in the Active Ionospheric Sounding (AIS) mode, MARSIS measures the propagation time delay of radar pulses with frequencies  $\sim 0.1$ – $5.5$  MHz from the spacecraft to the Martian ionosphere, where they are reflected as they enter the dense planetary plasma (Gurnett et al., 2005; Jordan et al., 2009; Picardi et al., 2004). The pulse sequence is repeated every 7.5 s while the instrument is active. Typically MARSIS is operated at altitudes below  $\sim 1,500$  km, although it is not activated in AIS mode during each periapsis pass. In AIS mode, MARSIS is also able to measure the local electron density, through the oscillations excited near the spacecraft at the local plasma frequency and its higher harmonics (Gurnett et al., 2005), albeit only during intervals when MEX is not located in fast flowing plasma regions and for electron densities  $n_e > \sim 10 \text{ cm}^{-3}$  (Duru et al., 2008). Furthermore, the local magnetic field magnitude at the spacecraft altitude can often be calculated from signals at the cyclotron frequency of accelerated electrons near the antenna (Gurnett et al., 2005). We emphasize that this measurement does not provide any information regarding the magnetic field vector. In this paper, only in-situ measurements from MARSIS in AIS mode are analyzed, using the highest possible measurement cadence of 7.5 s and processed as described by Andrews et al. (2013) and Andrews et al. (2015).

To obtain a clearer understanding of the processes controlling the structure of the Martian induced magnetosphere, upstream solar wind parameters need to be taken into account for a real time comparison. The necessary solar wind input is provided by SWIA and MAG onboard MAVEN (Halekas, Ruhunusiri, et al., 2017). SWIA measures ion density, temperature and velocity in the solar wind and magnetosheath within an energy range of 5 eV–25 keV and a time resolution of 4 s (Halekas et al., 2015), while the two fluxgate magnetometer sensors measure the vector magnetic field with a sample rate of 32 samples per second (Connerney et al., 2015). Preceding the aerobraking operations phase in early 2019, MAVEN's elliptical orbit permitted it to routinely sample the solar wind directly, although not continuously. Processing of these data on ground to improve the quality of the derived quantities further reduces their cadence to  $\sim 46$  s, averaging over the effects of upstream fluctuations with shorter timescales (Halekas, Ruhunusiri, et al., 2017). Intervals where the instrument did not directly sample the undisturbed (“pristine”) solar wind are excluded (Halekas, Ruhunusiri, et al., 2017). These measurements of solar wind density, velocity, and the IMF can be taken to provide

concurrent upstream driving conditions to compare to measurements from MEX, and their effects on the induced magnetosphere and ionosphere can be studied. We note that while MAVEN only encounters the pristine solar wind on  $\sim 60\%$  of all orbits (Halekas, Ruhunusiri, et al., 2017), the fraction of time for which MARSIS is operated in AIS mode on MEX is much smaller, less than 10% (Gurnett et al., 2005). Thus, intervals of simultaneous measurements remain relatively rare.

To demonstrate what we consider as simultaneous observations between the two-spacecraft throughout this paper, in Figure 1, we show as an example data from MEX orbit 14767 and MAVEN orbit 1754 obtained during Day Of Year (DOY) 235 and 236 in 2015. In Figures 1a and 1b, the energy spectrum and the density and speed of the pristine solar wind (Halekas, Ruhunusiri, et al., 2017) from SWIA on MAVEN are presented. In Figure 1c,

the magnetic field magnitude from MARSIS on MEX (Andrews et al., 2015) in the induced magnetosphere,  $|B|_{IM}$  (black dots), and the crustal magnetic field strength at the spacecraft location (blue line) based on the model by Cain et al. (2003), are shown. It can be seen that, close to periapsis at  $\sim 23:37$ , the measured magnetic field agrees closely with that predicted by the Cain et al. (2003) model, but deviates from it at higher altitudes where the relative contribution of the draped IMF becomes larger. For completeness, we also show those erroneous measurements of magnetic field strength that can clearly be seen to deviate from the general trends, both to higher and lower values, which we attribute to additional noise in the ionograms from which these values are ultimately derived. In Figures 1d and 1e the MEX and MAVEN trajectories in MSO coordinates are depicted as red and blue lines respectively in Mars radii units ( $1 R_M = 3389.5$  km) with  $\rho_{MSO} = \sqrt{Y_{MSO}^2 + Z_{MSO}^2}$ . The black segment on the red MEX orbit trace denotes the time during which MARSIS was operating in AIS mode, while the black boxes on the blue orbit show where MAVEN was located during the same interval. The dotted and dashed lines in Figure 1d represent the bow shock and MPB locations based on the model by Vignes et al. (2000). Comparing the trajectory plot of Figure 1d with Figures 1a and 1b, we notice that MAVEN happens to be located in the solar wind only for a few minutes during the MARSIS ionospheric passing.

The simultaneous data used in this study from these specific orbits are contained in the grey shaded region shown in Figures 1b and 1c. For each  $|B|_{IM}$  data point by MARSIS we look for the temporally closest solar wind observation by MAVEN within 300 s; when this condition is fulfilled we then consider this pair of observations as simultaneous, as illustrated with the grey shaded area in Figures 1b and 1c. If possible, that is, when solar wind measurements are available both before and after a MARSIS measurement, linear interpolation is also performed. Longer intervals of unavailable data, due, for example, to MAVEN leaving the undisturbed solar wind, MARSIS deactivating or switching out of AIS mode, or any other reason, are not further analyzed. Thus, when this approach is applied to the interval shown in Figure 1, only MARSIS data obtained within the grey shaded interval are further considered in this study, and all other data are rejected for further analysis. The 300 s upper limit applied as part of the selection of data is in part chosen to overcome atypical MARSIS operations schemes where the instrument is repeatedly switched between sub-surface and ionospheric sounding. It should be noted that this does not mean that the data are averaged in any way over this timescale; instead, the median elapsed time between individual MARSIS and SWIA measurements compared in this study is found to be  $\sim 16$  s, and the time interval between simultaneous pairs of data points does not exceed 300 s. We note that this approach differs somewhat from that used by Girazian et al. (2019) in analyzing data from both MAVEN and MEX, where average solar wind parameters were computed for an hour-long interval prior to the AIS data acquisition on each MEX orbit, and therefore variations in upstream conditions during the interval over which AIS data are acquired are not factored into their analysis. Furthermore, we note that a related analysis has been presented by Halekas, Brain, et al. (2017), in which the X-component of the magnetic field in the induced magnetosphere was compared to the upstream value, determined using single-spacecraft measurements.

To briefly illustrate the typical range and interdependencies of the upstream conditions, we summarize the solar wind and IMF measurements from MAVEN in Figure 2. Specifically, we show the correlations between the solar wind dynamic pressure ( $P_{dyn}$ , Figure 2a), speed ( $|v|_{sw}$ , Figure 2b) and density ( $n_{sw}$ , Figure 2c) with IMF ( $|B|_{IMF}$ ), as well as the anti-correlation between solar wind density and speed (Figure 2d). The Spearman's rank correlation coefficient,  $\rho$ , for the corresponding quantities has also been calculated and it is shown in each panel. In each case, only data taken in the pristine solar wind are shown, and the solar wind dynamic pressure is  $P_{dyn} = \rho_{sw} v_{sw}^2$ , where  $\rho_{sw}$  is the solar wind mass density and  $v_{sw}$  the solar wind velocity. Data are shown only for the interval from November 2014 to November 2018 during periods where MEX AIS measurements of the magnetic field magnitude were simultaneously available, as used in this study and demonstrated in the example orbits in Figure 1. The color-code in the four subplots represents the number of data points (N) per bin. The quantities depicted in Figure 2 ( $P_{dyn}$ ,  $|v|_{sw}$ ,  $n_{sw}$ ,  $|B|_{IMF}$ ) vary within their typical ranges. We observe a general trend of higher dynamic pressure corresponding to greater IMF magnitude values (Figure 2a), which is also seen in solar wind density (Figure 2c), whereas in the speed-IMF relationship (Figure 2b) no such trend is observed. Furthermore, the solar wind density and speed exhibit a degree of anti-correlation (Figure 2d).

Next, we proceed by examining the strength of the magnetic field measured in the induced magnetosphere at the location of MEX,  $|B|_{IM}$ , and comparing it to the instantaneous value of the unperturbed IMF at MAVEN location,  $|B|_{IMF}$ . The total magnetic field strength measured by MARSIS in the Martian ionosphere can be considered as the sum of the induced fields (i.e., the draped IMF), any crustal fields present at the location of the spacecraft,

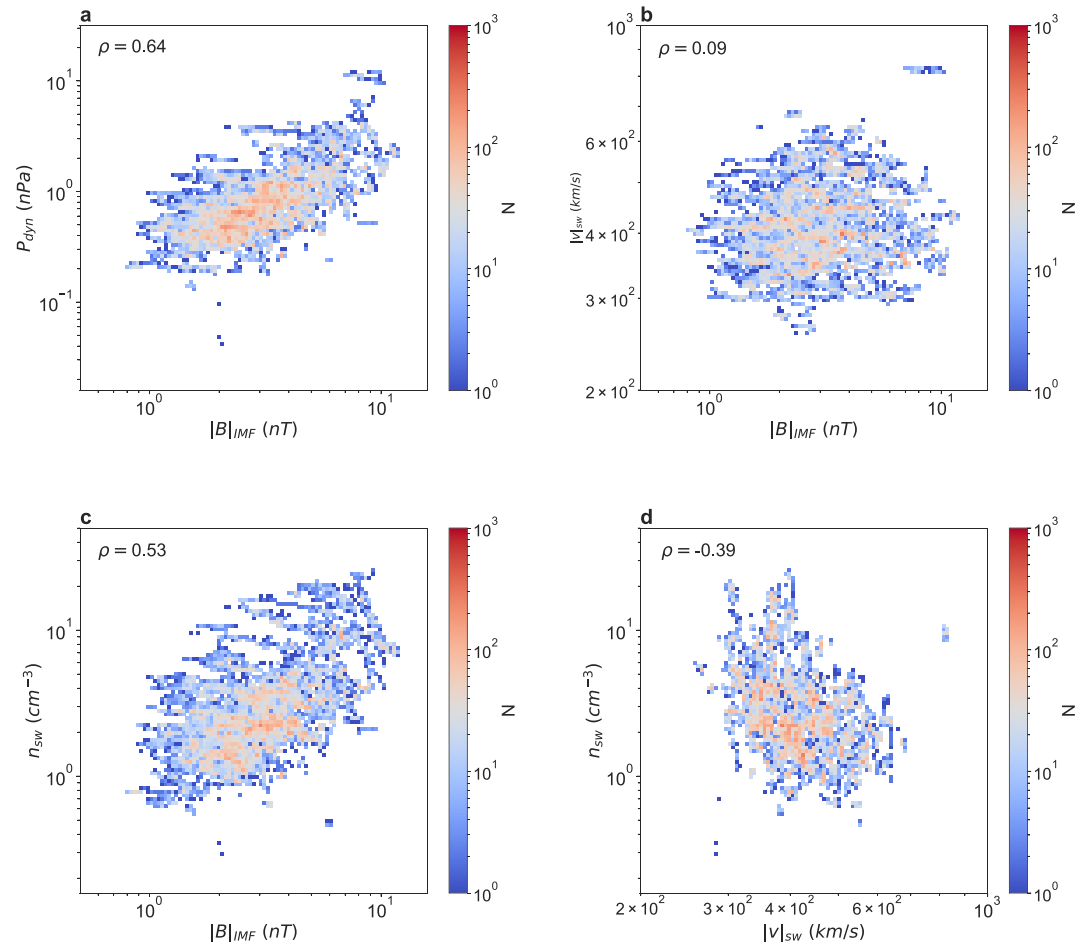


**Figure 2.** Correlation between (a)  $P_{\text{dyn}}$ , (b)  $|v|_{\text{sw}}$ , (c)  $n_{\text{sw}}$ , and IMF, and between (d)  $n_{\text{sw}}$  and  $|v|_{\text{sw}}$ . We only use data from SWIA and MAG from November 2014 to November 2018 during the periods for which simultaneous MEX MARSIS AIS magnetic field magnitude data were also available. The number of the data points per bin is displayed color-coded, and  $\rho$  is the Spearman's rank correlation coefficient of the corresponding quantities.

and any additional sources that may be present. However, since the measurements made are scalar in nature, there is no possibility to recover any of these individual physical contributions. For example, even though the crustal field is stable and well described by existing models, and there is therefore known a priori, neither the vector nor the magnitude of the remaining induced field (together with any other field sources) can be obtained by any physically justified operation on the measured total field. For completeness, we note that it is sometimes feasible to make an assumption of a purely horizontal, homogeneous induced field and obtain this vector by regression analysis when MEX crosses through regions of similarly intense crustal fields with large variations in orientation, as was done by Akalin et al. (2010). This approach is only viable though during a small selection of MEX orbits, and moreover yields only a single induced field vector per periapsis pass of MEX, and hence it is not suitable for the approach taken in this paper.

We examine the behavior of the  $|B|_{\text{IM}}/|B|_{\text{IMF}}$  ratio and thus we look at its correlation with  $P_{\text{dyn}}$  as well as with the Mach number, as a controlling factor of the IMF strength and the compression ratio across the shock. The Alfvén Mach number squared is given by the expression

$$M_A^2 = \frac{v_{\text{sw}}^2}{v_A^2} = \left( \frac{v_{\text{sw}} \sqrt{\mu_0 \rho_{\text{sw}}}}{|B|_{\text{IMF}}} \right)^2 = \frac{\mu_0 P_{\text{dyn}}}{B_{\text{IMF}}^2} \quad (1)$$

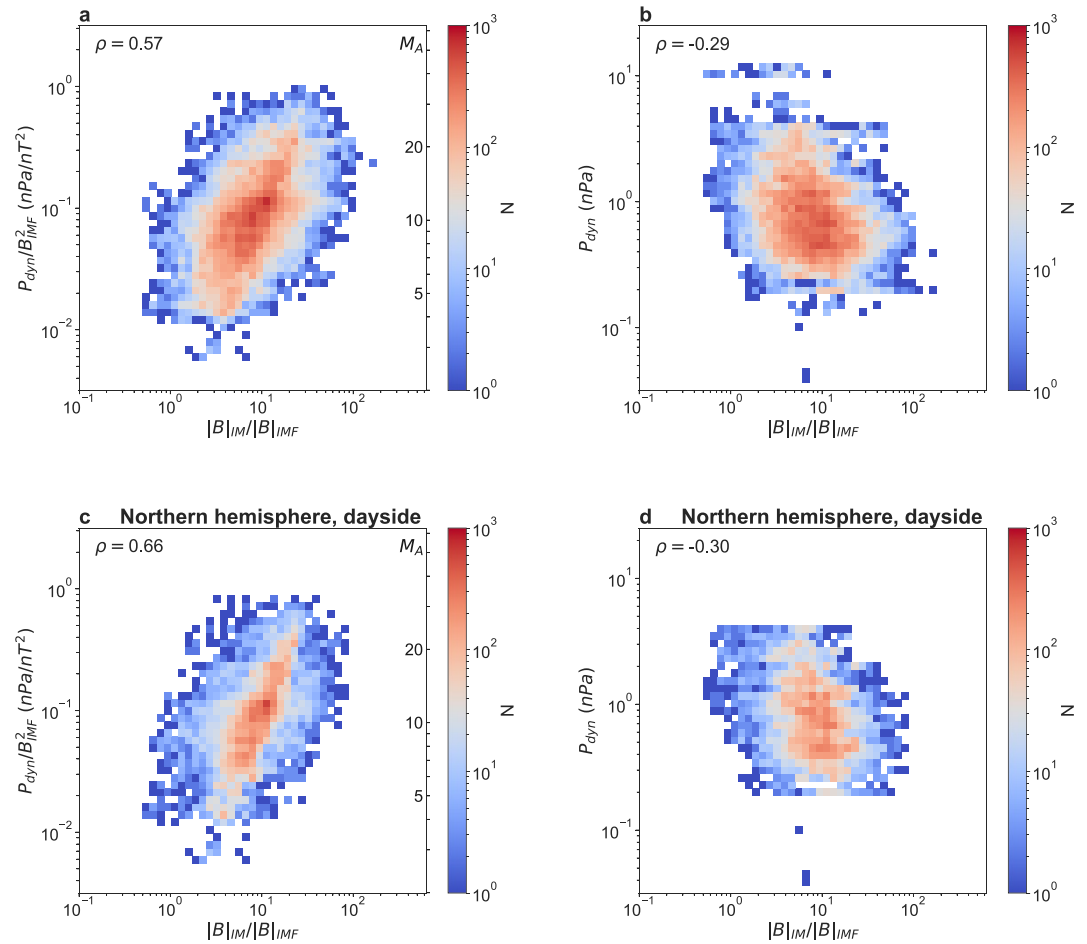


**Figure 3.**  $|B|_{IM}/|B|_{IMF}$  plotted versus (a),  $P_{dyn}/B_{IMF}^2$  (left axis) and  $M_A$  (right axis), and (b),  $P_{dyn}$  in 2D histograms where the number of data points ( $N$ ) is presented color-coded and Spearman's correlation coefficient is shown as  $\rho$ . The whole data set of simultaneous measurements is used in (a) and (b), whereas in (c) and (d) we show the same parameters only for the dayside of the northern hemisphere.

where  $v_A$  is the Alfvén speed,  $v_A = \frac{|B|_{IMF}}{\sqrt{\mu_0 \rho_{sw}}}$ ,  $\mu_0$  is the vacuum permeability and  $\rho_{sw}$  is the mass density considering only protons in the solar wind.

In Figure 3a we show how the  $|B|_{IM}/|B|_{IMF}$  ratio varies with  $P_{dyn}/B_{IMF}^2$  (left axis) and Mach number,  $M_A$  (right axis), and in Figure 3b we show  $|B|_{IM}/|B|_{IMF}$  against  $P_{dyn}$ . Figures 3c and 3d present the same parameters but for the northern hemisphere dayside only. In each subplot of Figure 3, Spearman's correlation coefficient,  $\rho$ , of the corresponding quantities is also shown. To calculate  $|B|_{IM}/|B|_{IMF}$ , we utilize magnetic field magnitude observations from MARSIS in the induced magnetosphere ( $|B|_{IM}$ ), derived with the cyclotron echo method (Andrews et al., 2015). We then divide each  $|B|_{IM}$  value with the simultaneous IMF ( $|B|_{IMF}$ ) as given by MAVEN in the solar wind (Halekas, Ruhunusiri, et al., 2017). In Figures 3a and 3b, measurements of  $|B|_{IM}$  are included irrespective of MEX's location, therefore variations in the induced field strength with position in the induced magnetosphere contribute to the broad scatter of the distributions shown, but nevertheless allow a first analysis of the general trends present. In particular, we note that MEX routinely encounters the strongest crustal field sources located in Mars' southern hemisphere, which will significantly contribute to the measured magnetic fields on the dayside, and often be dominant on the nightside where the induced fields are lower in intensity.

Hence, in the lower panels, in Figures 3c and 3d, we show equivalent plots to those above but now restricted to only dayside MEX measurements from the northern hemisphere. Figures 3c and 3d can therefore be directly compared with 3a and 3b, respectively, where the whole data set is utilized, and we note that there is no indication of crustal fields contributions significantly altering the overall picture of the correlation between the relative

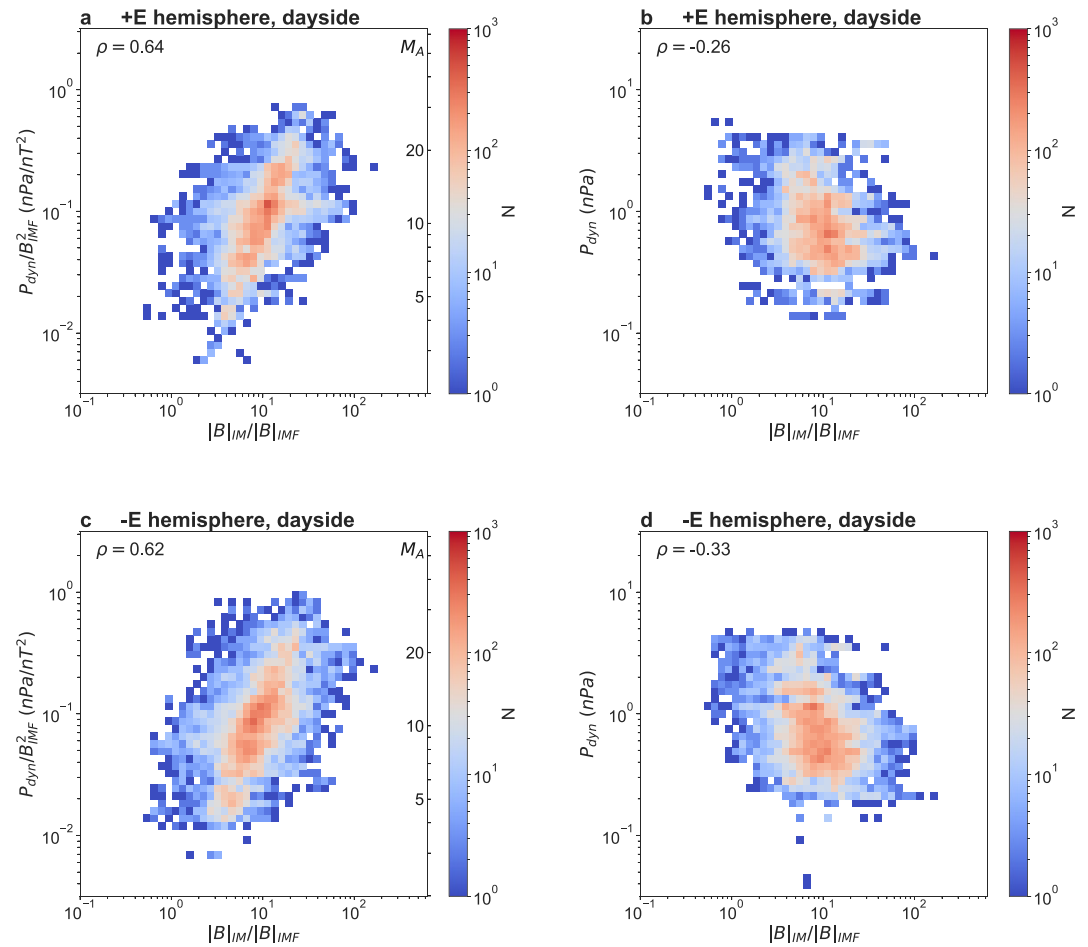


**Figure 4.** Data presented in a similar manner to Figure 3. Observations from the dayside of +E and the dayside of -E hemispheres have been used in (a), (b) and (c), (d) respectively.

magnetic field magnitude ratio, with Mach number and solar wind dynamic pressure. In both the entire data set shown in the top row, and in the restricted data set shown below, we observe greater ratio values for higher  $M_A$  in general (Figures 3a and 3c). However, when we plot the same ratio versus  $P_{dyn}$  in Figures 3b and 3d, the slope reverses, revealing opposite trends of the  $|B|_{IM}/|B|_{IMF}$  ratio with the  $M_A$  and  $P_{dyn}$ . Higher values of the ratio are therefore observed mostly during intervals of relatively lower dynamic pressures.

Many aspects of the Mars-solar wind interaction are controlled by the orientation of the motional electric field of the solar wind and IMF, present in the planet's frame (e.g., Halekas, Brain, et al., 2017). Such phenomena are best studied in the Mars Solar Electric (MSE) coordinate system, where the  $x$ -axis again is oriented toward the Sun and the IMF vector is contained in the  $x$ - $y$  plane with a positive  $y$  component. Thus “positive” (+E) and “negative” (-E) electric field hemispheres of interest are defined, based on the sign of the  $y$ -coordinate of the observer (MEX in this case). For each upstream measurement made by SWIA and MAG on MAVEN, a rotation from the MSO to MSE coordinate system can be obtained and applied to the positions of both MEX and MAVEN.

A division of the data set into the two solar wind electric field hemispheres follows in Figure 4, in which the relationship between  $|B|_{IM}/|B|_{IMF}$  and  $P_{dyn}/B_{IMF}^2$ ,  $M_A$  and  $P_{dyn}$  is presented in a similar format as in Figure 3. As in Figures 2 and 3, Spearman's correlation coefficient,  $\rho$ , is shown in each panel. The corresponding confidence widths (Bonett & Wright, 2000; Fisher, 1921) for each pair of variables plotted in Figures 2–4 were also computed (not shown in the figures). In the majority of the cases, the confidence width of  $\rho$  is no greater than 0.02, while for a few pairs of variables it reaches 0.03, meaning that random samples of the same data would return a correlation coefficient within this range 95% of the time. Here, only data obtained on the dayside are included, where control by the motional electric field is anticipated to be most effective owing to the greater penetration of this field into

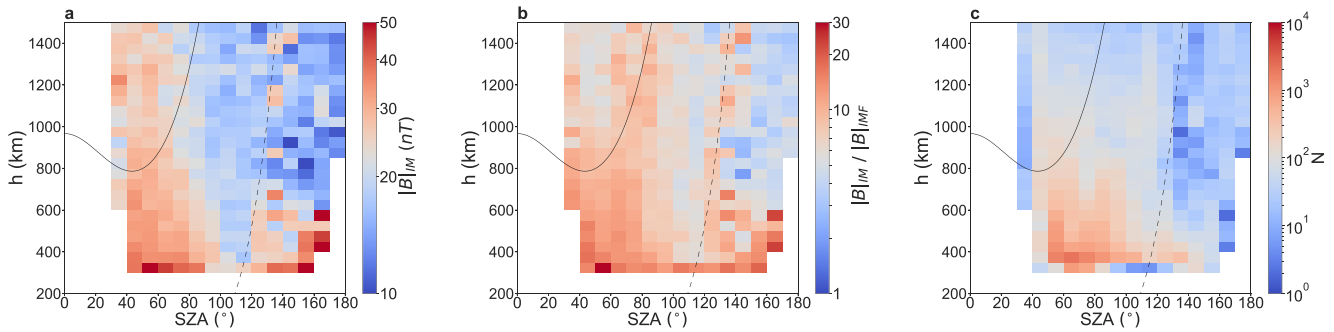


**Figure 5.**  $|B|_{IM}$  and  $|B|_{IM}/|B|_{IMF}$  plotted color-coded for different altitudes and SZAs of MEX's orbit (Figures 5a and 5b) and the corresponding data set coverage (Figure 5c). The solid black line displays the MPB, based on the model by Vignes et al. (2000), and the dashed black line shows the location of the optical shadow. The binning of the SZA and altitude is  $10^{\circ}$  and 50 km, respectively.

the induced magnetosphere. The term dayside, in Figures 3 and 4, corresponds to observations that come from regions with solar zenith angle no greater than  $90^{\circ}$  ( $SZA < 90^{\circ}$ ). In general, the correlation between the ratio and the Mach number (Figures 4a and 4c) as well as the ratio and the dynamic pressure (Figures 4b and 4d) follow the same trends already observed in the MSO frame previously in Figure 3. Comparing the results obtained in the two opposing electric field hemispheres ( $+E$ ,  $-E$ ) within each column of Figure 4, the spread and the resulting correlations within the measurements do not seem to differ importantly, indicating the solar wind electric field not being a crucial aspect when investigating the magnetic field magnitude enhancement in the induced magnetosphere as a function of Mach number and the dynamic pressure. Any minor differences that may be noted between the results obtained in the opposing hemispheres and departures from the trends observed earlier in Figure 3 are likely due to the further separation of the data into sub-sets.

In order to introduce the general structure of the magnetic field magnitude of the upper ionosphere, the same data are now analyzed in the altitude–SZA coordinate system appropriate to studying spatial variations in the induced magnetosphere. Specifically, we show in Figure 5a the magnetic field magnitude in the induced magnetosphere  $|B|_{IM}$ , (b) the  $|B|_{IM}/|B|_{IMF}$  ratio utilizing again simultaneous IMF measurements as previously described, and (c) the coverage of the simultaneous MEX and MAVEN data, with the total number of simultaneous pairs of MEX and MAVEN data points being 42,395. These values are computed in spatial bins of 10 degrees of SZA and 50 km of altitude, offering reasonable resolution in both directions whilst retaining a sufficient number of typical measurements per bin. In each panel, the black solid line depicts the MPB location based on the model by Vignes et al. (2000), while the dashed black line indicates the optical shadow boundary (equivalent to the terminator at the surface).

In Figure 5a, where the induced magnetospheric fields caused by the interaction with the solar wind are presented, we observe magnetic fields of a few tens of nT in the dayside which decrease in magnitude slowly with increasing altitude and are notably of similar magnitude both below and above the nominal MPB. The magnetic field magnitude drops toward the shadowed nightside and the surrounding region ( $SZA \sim 90^{\circ} - 130^{\circ}$ ). There is some suggestion that immediately following the transition into shadow, in some bins the field strength is observed to increase, possibly indicative of a more complex interaction between the draped fields and the ionosphere. This may either be attributed to more localized fields associated with the tail current sheet, or could also be the result of the apparent twist in the magnetotail configuration caused by magnetic reconnection between the IMF and crustal fields (DiBraccio et al., 2018; Xu et al., 2020). An additional contribution, present only at low altitudes in the nightside, stems from the crustal fields which, depending on the specific planetocentric location of the underlying observations, may be the dominant contribution to the measured fields. These crustal fields necessarily decrease in strength rapidly with altitude, much faster than the draped fields on the dayside. As discussed by Andrews et al. (2015), the local magnetic field magnitude can only be reliably determined by AIS if it lies in the range  $\sim 5$ –200 nT, owing to the (range) resolution of the sounder. Further issues of sensitivity may also be expected in regions of particularly low plasma density. We note also that the ionospheric mode of MARSIS is favored mostly for dayside operations, whereas on the nightside it is often switched off to facilitate subsurface observations for altitudes lower than  $\sim 800$  km (Picardi et al., 2004). Cumulatively, given that the quantities plotted in Figures 5a and 5b are mean values, these effects necessarily lead to the larger relative contribution of the

more intense crustal field sources at low altitudes on the nightside, as compared to the much weaker or indeed generally absent draped IMF, or fields associated with the induced magnetotail at the same location. As discussed previously, it is not possible to separate draped or induced magnetic fields from crustal sources, given the scalar nature of the measurements by MARSIS.

In Figure 5b we directly compare the induced fields to the instantaneous fields of the upstream IMF, plotting the ratio of the magnetic field magnitude from MEX over the IMF measured simultaneously ( $|B|_{\text{IM}}/|B|_{\text{IMF}}$ ), corresponding to the data shown first in Figure 3b. The large scale variations of the ratio of these field magnitudes can be seen in Figure 5b to be rather different from those of the mainly induced (draped) fields considered in isolation as shown in Figure 5a. On the dayside for  $\text{SZA} < 90^\circ$ , and at altitudes below  $\sim 900$  km corresponding to the nominal MPB, a region where  $|B|_{\text{IM}} \gg |B|_{\text{IMF}}$  is present. However, a decrease in this ratio with altitude above the MPB is now apparent. A further sharp drop in the observed ratios at SZAs above  $\sim 90^\circ$  divides the examined region into two parts, and the lowest observed ratios are found beyond the optical shadow boundary. There does also appear to be some evidence of locally enhanced ratios scattered at and slightly anti-sunward of the optical shadow boundary itself, although this is only confined to a few bins and may simply be due to random variation in the underlying data. While some suggestion of this enhancement was detected in a few individual bins at the same locations in Figure 5a, the effect is much clearer in the ratios shown in Figure 5b. The same enhancement in the ratio at the lowest altitudes shown on the nightside is again present, owing to the contribution of crustal magnetic field sources to the measurements in the absence of significant draped IMF fields in this region.

In Figure 5c, for reference, the corresponding coverage of the simultaneous MEX and MAVEN observations is shown in the time interval between November 2014 and November 2018. A strong bias toward the dayside and a relatively undersampled upper nightside due to the additional condition of available contemporaneous solar wind MAVEN data is observed, indicating the relative strength of the conclusions that can be drawn regarding the trends seen in different regions of the induced magnetosphere.

Having established the overall magnetic field structure of the upper ionosphere, we proceed to investigate how it varies with upstream solar wind conditions. In Figure 6, we re-analyze the same data already presented, by dividing it into three groups defined by the upper, lower and inter-quartile ranges of three solar wind parameters, namely the solar wind dynamic pressure (Figures 6a–6f), speed (Figures 6g–6i) and density (Figures 6j–6l). While further sub-divisions of the data were also examined, the limitations of coverage both in altitude and SZA, and indeed season, latitude and local time generally preclude drawing conclusions due to biases introduced.  $|B|_{\text{IM}}$  and  $|B|_{\text{IM}}/|B|_{\text{IMF}}$  for low ( $P_{\text{dyn}} < 0.5$  nPa), intermediate ( $0.5 \text{ nPa} < P_{\text{dyn}} < 1.1$  nPa) and high solar wind dynamic pressure ( $P_{\text{dyn}} > 1.1$  nPa) are presented in Figures 6a and 6d, 6b and 6e, and 6c and 6f respectively, with the format otherwise derived from that used in Figure 5. More intense induced fields are observed in the dayside during periods of high solar wind dynamic pressure, as shown in the three upper plots (Figures 6a–6c), consistent with the pressure balance expected between the induced magnetosphere and the upstream solar wind, illustrating the ability of the induced magnetosphere to adjust to varying solar wind conditions. Comparing the induced fields relative to the IMF however, a different picture emerges, as is evident in Figures 6d–6f. The induced fields are readily seen to be relatively more intense compared to the IMF during intervals of low dynamic pressure in the dayside and in the region immediately surrounding the nominal MPB. Counterintuitively therefore, while the IMF itself is (typically) increased in magnitude during intervals of higher solar wind dynamic pressure (Figure 2a), the induced fields in the dayside ionosphere are observed to be stronger relative to the IMF during intervals of lower dynamic pressure. (We emphasize that this is consistent with the results already discussed for the same data analyzed as a whole and presented in Figures 3 and 4.)

In Figures 6g–6l, we examine variations with the contributing separate terms to the dynamic pressure, namely the solar wind speed and density. Specifically, we show only the ratios of field strengths  $|B|_{\text{IM}}/|B|_{\text{IMF}}$  for low ( $v_{\text{sw}} < 362 \text{ km s}^{-1}$ ), intermediate ( $362 \text{ km s}^{-1} < v_{\text{sw}} < 458 \text{ km s}^{-1}$ ) and high ( $v_{\text{sw}} > 458 \text{ km s}^{-1}$ ) speed values, in Figures 6g, 6h and 6i and for low ( $n_{\text{sw}} < 1.7 \text{ cm}^{-3}$ ), intermediate ( $1.7 \text{ cm}^{-3} < n_{\text{sw}} < 3.9 \text{ cm}^{-3}$ ) and high ( $n_{\text{sw}} > 3.9 \text{ cm}^{-3}$ ) solar wind density, in Figures 6j, 6k and 6l, respectively. While there are no significant differences in the structure of the ratios between the cases of slow and fast solar wind (Figures 6g and 6i, respectively), the solar wind density seems to influence the relative induced fields in a similar fashion to dynamic pressure, that is to say producing an enhanced ratio for low solar wind density in the dayside and the MPB region. This is also supported by the power-law relationship between both the solar wind dynamic pressure and density, and the IMF we see in Figures 2a and 2c.

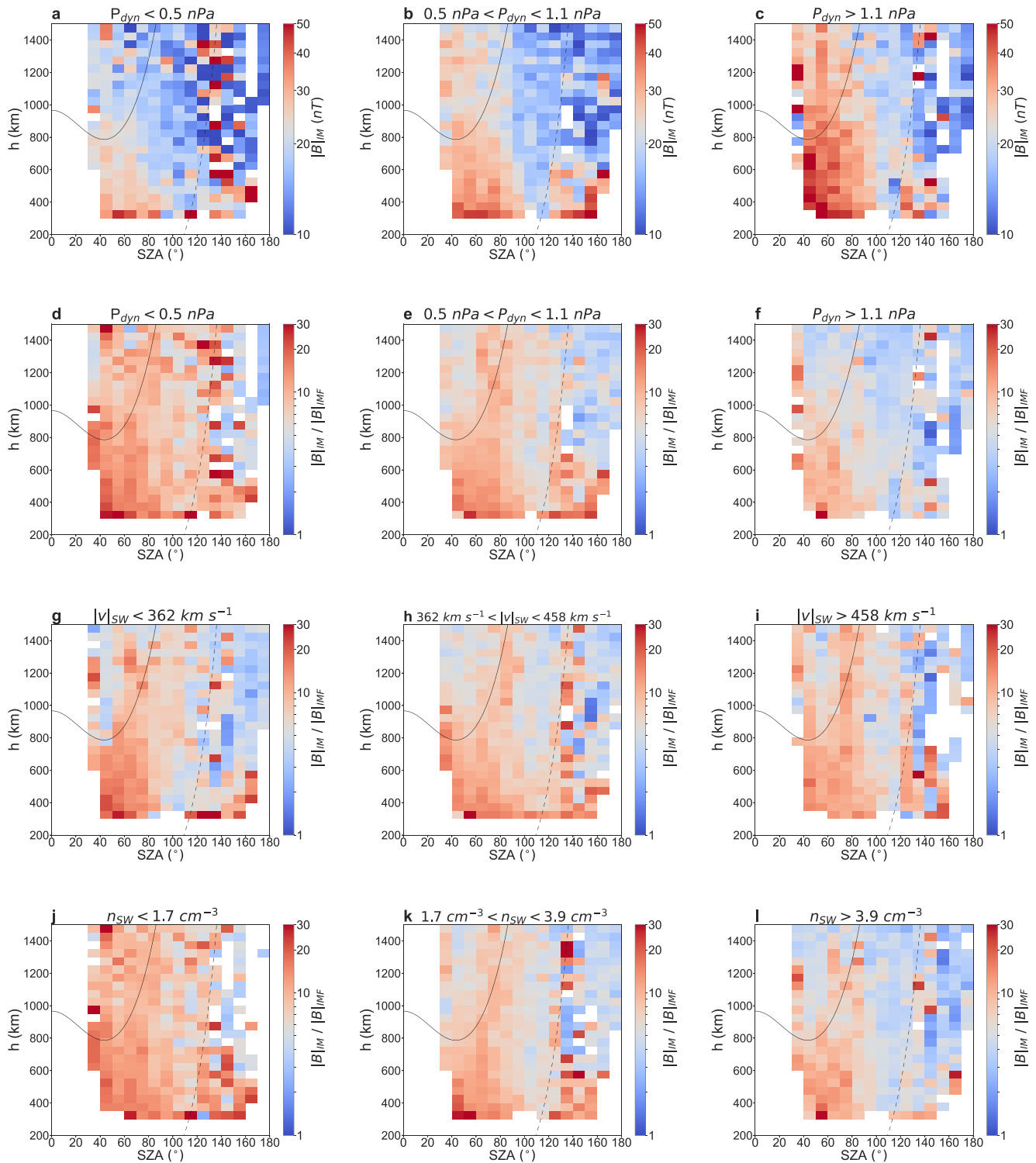


**Figure 6.** Magnetic field magnitude from MEX ( $|B|_{IM}$ ) in SZA-altitude diagrams for low, intermediate and high  $P_{dyn}$  (Figures 6a–6c), and  $|B|_{IM}/|B|_{IMF}$  for low, intermediate and high  $P_{dyn}$  (Figures 6d–6f), slow, intermediate and fast solar wind (Figures 6g–6i) and low, intermediate and high solar wind density (Figures 6j–6l), respectively. The criteria applied (lower and upper quartiles for each parameter) to the upstream solar wind conditions are given above each panel, and the format of each panel is otherwise identical to that used in Figure 5.

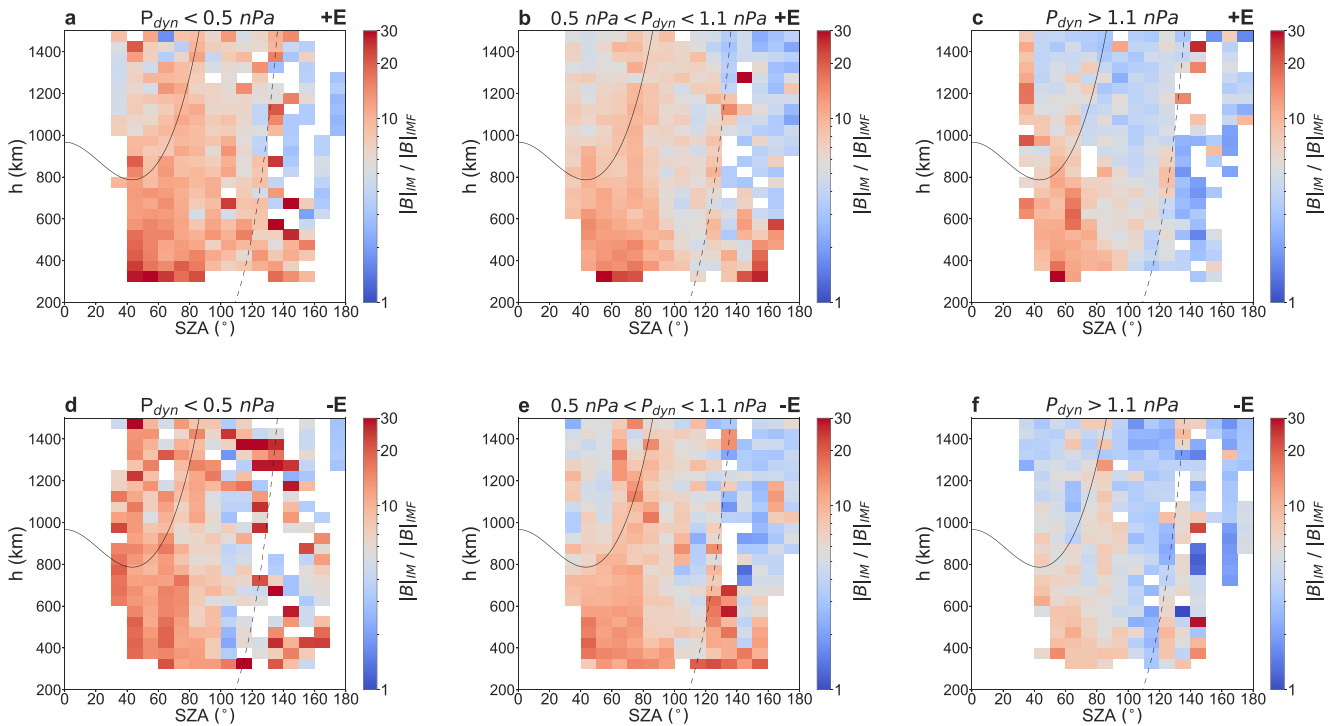


**Figure 7.**  $|B|_{IM}/|B|_{IMF}$  in SZA-altitude diagrams for low (Figures 7a and 7d), intermediate (Figures 7b and 7e) and high (Figures 7c and 7f)  $P_{dyn}$  respectively. Measurements coming only from the +E hemisphere are presented in Figures 7a–7c, while observations from the –E hemisphere are plotted in Figures 7d–7f. The criteria applied (lower and upper quartiles for  $P_{dyn}$  in each electric field hemisphere) are given above each panel.

To ensure that the solar wind electric field does not play a key role, as the dynamic pressure does, in determining the ratio of the field strengths at a given location, we plot again  $|B|_{IM}/|B|_{IMF}$  in SZA - altitude diagrams for low, intermediate and high  $P_{dyn}$ , but this time we divide the dataset into the positive and negative electric field hemispheres as depicted in Figures 7a–7c and 7d–7f, respectively. In the lower pressure regime, a higher ratio is seen in the upper ionosphere in the –E hemisphere, while for intermediate SZAs (80°–120°) the ratio is greater in the +E hemisphere (Figures 7a and 7d). The ratio seems to be more enhanced in the dayside in the +E hemisphere for high solar wind dynamic pressure (Figures 7c and 7f), however for intermediate values of dynamic pressure, besides moderate local enhancements near the MPB in the upper ionosphere in the –E hemisphere, the distribution of the ratio values around Mars is rather similar in the two plots (Figures 7b and 7e). Despite these differences in the ratio between +E and –E, the overall tendency of  $|B|_{IM}/|B|_{IMF}$  being noticeably more enhanced for low dynamic pressures can be clearly observed in both electric field hemispheres in Figure 7.

In Tables 1 and 2, we show the mean and the standard error of the mean (mean  $\pm$  SEM) of the strength of the magnetic field in the induced magnetosphere ( $|B|_{IM}$ ) and the relative ratio over the IMF ( $|B|_{IM}/|B|_{IMF}$ ) respectively, first for the whole dataset subdivided into different regions based on the optical shadow, latitude (northern or southern hemisphere) and the solar wind electric field, and then for the subsets of low, intermediate and high  $P_{dyn}$  as they result from the quartile partitions and have been used in Figures 6 and 7, again subdivided into the same regions as before. The term dayside here (Tables 1 and 2) is used for measurements only from sunlit regions and altitudes below the MPB.

Looking at Table 1, the mean  $|B|_{IM}$  for the total group of measurements is as expected greater in the dayside than the nightside and also in the southern hemisphere than the northern due to the contribution of the crustal fields. What is more, we see generally higher values of  $|B|_{IM}$  in the +E hemisphere, both on the dayside irrespective of latitude and when we restrict northern latitudes only (where any direct influence of crustal field sources is minimized). The same behavior among the different regions is observed too, for the low, intermediate and high  $P_{dyn}$  regimes, although comparatively, for low  $P_{dyn}$  the magnetic field magnitude appears to diverge much less. Moreover, the expected correlation between high solar wind dynamic pressure and stronger fields becomes apparent when we compare the columns of low and high  $P_{dyn}$  for every sub-region except for the nightside. Thus, if we

**Table 1**

Mean and Standard Error of the Mean (SEM) of  $|B|_{IM}$  (nT) for the Whole Dataset and for Low, Intermediate and High  $P_{dyn}$  for Various Subdivisions of the Dataset Based on the Optical Shadow, Latitude and Solar Wind Electric Field

$ B _{IM}$ (nT)	Mean $\pm$ SEM (nT)			
	Total	Low $P_{dyn}$	Intermediate $P_{dyn}$	High $P_{dyn}$
All data	27.8 $\pm$ 0.1	23.5 $\pm$ 0.1	27.9 $\pm$ 0.1	32.0 $\pm$ 0.2
Dayside	28.8 $\pm$ 0.1	23.7 $\pm$ 0.2	28.9 $\pm$ 0.1	33.5 $\pm$ 0.2
Nightside	22.9 $\pm$ 0.3	23.1 $\pm$ 0.6	23.4 $\pm$ 0.4	21.6 $\pm$ 0.5
Dayside, +E hem.	30.4 $\pm$ 0.1	24.1 $\pm$ 0.2	31.0 $\pm$ 0.2	35.6 $\pm$ 0.3
Dayside, -E hem.	27.4 $\pm$ 0.1	23.3 $\pm$ 0.2	27.2 $\pm$ 0.2	31.7 $\pm$ 0.2
Dayside, Northern hem.	27.0 $\pm$ 0.1	22.3 $\pm$ 0.2	26.3 $\pm$ 0.1	32.9 $\pm$ 0.2
Dayside, Southern hem.	31.1 $\pm$ 0.2	25.1 $\pm$ 0.3	32.3 $\pm$ 0.3	34.5 $\pm$ 0.3
Dayside, Northern, +E hem.	28.4 $\pm$ 0.1	22.9 $\pm$ 0.2	27.7 $\pm$ 0.2	35.5 $\pm$ 0.3
Dayside, Northern, -E hem.	25.4 $\pm$ 0.1	21.8 $\pm$ 0.3	25.0 $\pm$ 0.2	29.9 $\pm$ 0.3

only look at the dayside, there is a  $\sim 41\%$  increase of the mean  $|B|_{IM}$ , consistent with expectations from pressure balance given the increase of the dynamic pressure magnitude.

In Table 2, the mean relative ratio  $|B|_{IM}/|B|_{IMF}$  of the whole data set is greater in the dayside and the southern hemisphere compared to the nightside and the northern hemisphere, respectively. Even though the ratio appears to be higher in the +E hemisphere in the whole dayside, there seems to be no difference between the two electric field hemispheres in the northern dayside hemisphere. In the dayside in the northern hemisphere, the ratio reaches larger values in the -E region for low  $P_{dyn}$ , and in the +E region for high  $P_{dyn}$ . In both northern and southern hemispheres the mean ratio remains approximately the same for high  $P_{dyn}$ . Opposite to the picture presented in Table 1 (and in Figures 6a–6c), the mean ratio is greater for low  $P_{dyn}$  in all cases even in the nightside as it has been presented in Figures 6d–6f and 7. We find a decrease of  $\sim 36\%$  and  $\sim 39\%$  of the mean ratio in the dayside and in the whole data set, respectively from low to high  $P_{dyn}$ .

### 3. Discussion

A two-spacecraft study with combined measurements from the induced magnetosphere and the unperturbed solar wind is conducted, in an attempt to further illuminate the processes controlling the structure of the Martian near-space environment. Simultaneous data, chosen as illustrated in Figure 1, of magnetic field magnitude from MEX and IMF from MAVEN allows us a real time comparison of the magnetospheric response to solar wind parameters. The statistical distribution of the solar wind measured by MAVEN during the interval examined,

**Table 2**

Mean and Standard Error of the Mean (SEM) of  $|B|_{IM}/|B|_{IMF}$  Calculated and Presented in a Similar Manner as in Table 1

$ B _{IM}/ B _{IMF}$	Mean $\pm$ SEM			
	Total	Low $P_{dyn}$	Intermediate $P_{dyn}$	High $P_{dyn}$
All data	10.0 $\pm$ 0.1	12.0 $\pm$ 0.1	10.3 $\pm$ 0.1	7.3 $\pm$ 0.1
Dayside	10.6 $\pm$ 0.1	12.4 $\pm$ 0.1	11.1 $\pm$ 0.1	7.9 $\pm$ 0.1
Nightside	7.8 $\pm$ 0.1	10.0 $\pm$ 0.3	8.0 $\pm$ 0.2	5.1 $\pm$ 0.1
Dayside, +E hem.	11.1 $\pm$ 0.1	12.6 $\pm$ 0.1	11.4 $\pm$ 0.1	8.8 $\pm$ 0.1
Dayside, -E hem.	10.2 $\pm$ 0.1	12.2 $\pm$ 0.1	10.8 $\pm$ 0.1	7.1 $\pm$ 0.1
Dayside, Northern hem.	9.8 $\pm$ 0.1	11.8 $\pm$ 0.1	9.7 $\pm$ 0.1	7.9 $\pm$ 0.1
Dayside, Southern hem.	11.7 $\pm$ 0.1	13.1 $\pm$ 0.2	12.9 $\pm$ 0.1	7.8 $\pm$ 0.1
Dayside, Northern, +E hem.	9.8 $\pm$ 0.1	11.6 $\pm$ 0.1	9.7 $\pm$ 0.1	8.4 $\pm$ 0.1
Dayside, Northern, -E hem.	9.7 $\pm$ 0.1	12.2 $\pm$ 0.2	9.7 $\pm$ 0.1	7.3 $\pm$ 0.1

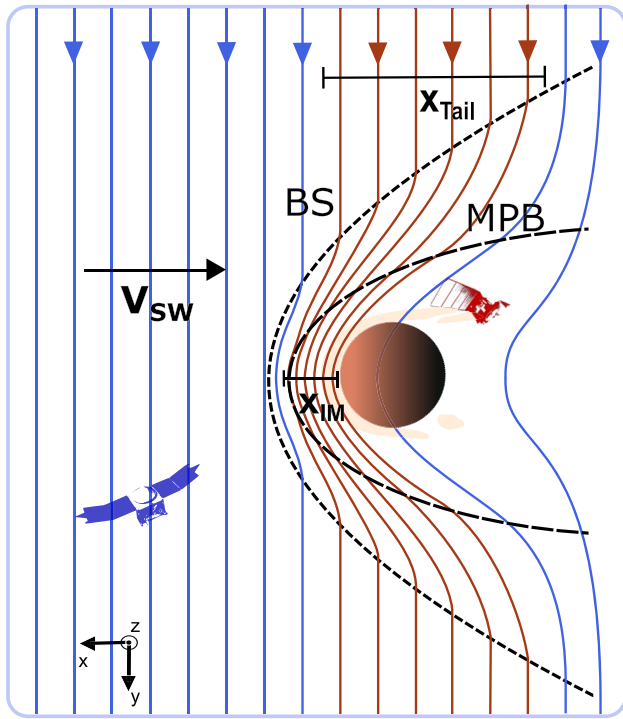


**Figure 8.** Mars-Solar wind interaction in MSO coordinates. The field lines of the IMF are shown in blue, whereas those field lines that thread the induced magnetosphere on the dayside are displayed in red. The boundary distances (BS-MPB-ionosphere) are not shown to scale. The blue and red spacecraft are MAVEN and MEX, respectively.

constrained also to the periods immediately surrounding MARSIS operations in AIS mode, was shown in Figure 2. Utilizing measurements of the local magnetic field magnitude made by MARSIS, we have examined the induced magnetosphere's structure and variation with upstream conditions, both in terms of the absolute induced fields and relative to the upstream IMF.

To highlight how variations in the strength of the magnetic field in the induced magnetosphere correspond to variations in the volume of the solar wind region it is linked to, we illustrate, in Figure 8, the Mars-Solar wind interaction in which field lines of the IMF (blue lines) are incident on the system and pile up at and above the dayside ionosphere. This illustration is drawn in the Mars Solar Orbital (MSO) frame, where  $X_{\text{MSO}}$  points from Mars to the center of the Sun,  $Y_{\text{MSO}}$  is opposite to the direction of Mars' orbital velocity and  $Z_{\text{MSO}}$  completes the right-handed system. The bow shock and MPB, where MPB is considered to be the lower edge of the magnetosheath as previously stated, are also depicted, though for the sake of clarity, they are not shown to scale with the planet. The situation displayed is heavily simplified as no component of the IMF along the Mars-Sun line is included (i.e.,  $B_x = 0$ ), and no interactions with the crustal fields have been considered. In reality, both factors will routinely distort the depicted draped field lines to greater or lesser degrees depending on the precise circumstances. The pile-up of the IMF field lines occurs as their motion past and through the ionospheric obstacle is slowed, and as a consequence, the field strength in the induced magnetosphere is significantly enhanced relative to the unperturbed solar wind. Field lines that can be considered to be part of the induced magnetosphere, crossing the MPB and therefore having at least some extent within the MPR, are shown as red lines. We note that an additional, smaller enhancement to the field strength also occurs in the immediately post-shocked IMF, where the slowing (and heating and diversion) leads to compression of the field lines with a limiting theoretical relative enhancement of a factor 4 (Russell et al., 2016). The linear extent of the induced magnetosphere on the

Sun-Mars line,  $X_{\text{IM}}$ , is indicated in the figure by the horizontal black bar. This is taken to be the altitude of the MPB at the subsolar point, and those IMF field lines that pass through this region are shown red. The horizontal extent of the region threaded by these same field lines in the otherwise undisturbed solar wind,  $X_{\text{Tail}}$ , is indicated by the longer black bar, across which all the red-colored IMF field lines pass. Following the definitions adopted in this paper for the MPB and MPR, we correspondingly define  $X_{\text{IM}}$  to be the altitude of the MPB at the sub-solar point. It should be noted, however, that the nature of the MPB, which in some sense is more akin to a transition between plasma regimes and is not therefore vanishingly thin compared to the magnetosheath and MPR above and below it, makes these definitions somewhat arbitrary. As depicted, the regions  $X_{\text{IM}}$  and  $X_{\text{Tail}}$  are therefore magnetically linked and to first-order, consideration of conservation of magnetic flux gives a simple relationship between the ratio of the field strength of the induced magnetosphere,  $|B|_{\text{IM}}$ , and the unperturbed upstream field  $|B|_{\text{IMF}}$  that can be compared to the ratio of these two length scales,

$$\frac{|B|_{\text{IM}}}{|B|_{\text{IMF}}} = \frac{X_{\text{Tail}}}{X_{\text{IM}}}. \quad (2)$$

While the MPB is well known to expand and contract with variations in upstream conditions (i.e., Edberg et al., 2009; Němec et al., 2020) the amplitude of this variation is only of the order of 15% in linear scale at the subsolar point over the typical range of dynamic pressures experienced at Mars (Němec et al., 2020). Thus, as the ratio of the fields increases, and the piled up field strength is observed to increase relative to the unperturbed IMF, the implication is that the horizontal extent of the interaction region is increased, with IMF field lines further down the tail remaining connected to the dayside induced magnetosphere. The situation illustrated in Figure 8 is a simplification as non-zero  $B_x$  and  $B_z$  components in the IMF will distort the picture. Furthermore, magnetic fields produced by ionospheric currents in the deep Martian ionosphere (e.g., Fillingim et al., 2012; Withers et al., 2005) are not considered here, and that approach is not suitable for intervals where the  $B_x$  component in the

IMF dominates. Nevertheless, this serves to illustrate the relationship that may be expected between the strength of the magnetic field in the dayside induced magnetosphere, and the spatial extent in the solar wind of the IMF flux tubes threading this region.

As illustrated in Figure 8, the field lines comprising Mars' induced magnetosphere are those of the IMF, slowed during their passage through the conductive upper ionosphere and around the obstacle. Hence, the increase in the magnetic field strength in the induced magnetosphere,  $|B|_{\text{IM}}$ , measured by MEX, can be compared to the strength of the unperturbed IMF  $|B|_{\text{IMF}}$ , measured by MAVEN. The ratio  $|B|_{\text{IM}}/|B|_{\text{IMF}}$  provides a simple indication of the relative compression or expansion of the induced magnetosphere, being related to the length scale over which IMF field lines are perturbed in their passage around and through the Martian ionospheric obstacle (with higher ratios indicative of a relatively expanded system, and vice-versa). In Figures 3 and 4, we first examined the correspondence between the ratio of these two measured field strengths, and upstream values of the solar wind dynamic pressure and Alfvén Mach number (proportional to the ratio of the dynamic pressure to the IMF strength squared). This comparison, initially made irrespective of MEX's position within the induced magnetosphere, showed the expected dependence, with the relative magnetic fields rising with increasing Alfvén Mach number, and falling with increasing dynamic pressure. We then sub-divide these data into both observations made only in the northern hemisphere and on the dayside, where any potential influence of crustal fields is minimized, and also into the +E and −E hemispheres in the MSE coordinate system, again restricting them to the dayside only. In both cases, no significant departures from the general trends are evident, strongly suggesting that both the crustal fields and the local orientation of the motional electric field play only minor roles, on average, in establishing the induced magnetosphere and modulating its response to variations in the upstream conditions. The mass loading of the solar wind by escaping planetary ions is known to be asymmetric (e.g., Dong et al., 2015) as fluxes are significantly higher in the +E hemisphere, and a related effect has been noted in the form of the induced magnetic fields (e.g., Dubinin et al., 2019). However, the data presented in Figure 4 shows that the same trends in the variation of the ratio  $|B|_{\text{IM}}/|B|_{\text{IMF}}$  with upstream conditions are present in both the +E and −E hemispheres.

The large-scale structure of the induced magnetosphere, as defined by the observed induced field strengths observed by MARSIS shown in Figure 5a is found to be in agreement with previous related studies (Akalin et al., 2010; Girazian et al., 2019), specifically showing enhanced field strengths on the dayside that gradually fall with increasing altitude. The response of the induced magnetosphere to intervals of relatively enhanced solar wind dynamic pressure leads to the enhancement of the induced fields, in absolute magnitude, most clearly on the dayside as shown in Figures 6a–6c.

However, when the induced field is instead again analyzed relative to the instantaneous value of the IMF by calculating the ratio  $|B|_{\text{IM}}/|B|_{\text{IMF}}$ , a rather different picture emerges, particularly when examining the response of this quantity to factors such as the solar wind dynamic pressure, speed, and density. As noted, while the magnetic field magnitude in the induced magnetosphere measured by MEX increases during the high  $P_{\text{dyn}}$  periods (Figure 6c), when we compute the ratio  $|B|_{\text{IM}}/|B|_{\text{IMF}}$  we find instead reduced relative induced fields for high solar wind dynamic pressure, mainly on the dayside and up to the nominal MPB region (Figure 6f). Moreover, while the averaged values of the induced fields observed by MEX on the dayside do not appreciably vary in any way at or near the nominal MPB location, as seen in Figure 5a, the ratio of the induced to IMF field,  $|B|_{\text{IM}}/|B|_{\text{IMF}}$ , does appear to show more organization by this boundary, with typically higher values found immediately below the boundary than above. This could perhaps be taken as a signature of currents flowing near or below the boundary, acting to enhance the induced fields below and reducing them above, thus bearing at least some outward similarity to the magnetopause at the Earth, as shown recently by Ramstad et al. (2020). We note that the analysis presented here only completely covers the region of SZAs from 40 to 160° at the periapsis altitude of MEX, and hence these conclusions are only supported by observations in this region. However, based on related studies of the structure of the magnetic fields closer toward the sub-solar point, which find field strengths that vary only weakly on average with SZA below 45° (Akalin et al., 2010), we see no reason not to at least cautiously extrapolate the central results of this study to lower SZA as well.

Turning to the tail, the induced (draped) field strength tentatively rises in strength immediately following the transition into shadow, as seen in Figure 5a, likely indicative of the more dynamic aspects of the Martian induced magnetotail as reported elsewhere, and suggesting that the fields observed in the tail are not purely those of the draped IMF. However, systematic effects here arising from the somewhat indirect measurement of the local field strength by MARSIS may distort this picture and cannot immediately be ruled out, given the rather different bulk

plasma conditions at these altitudes on the nightside as compared to the dayside. We again observe relatively higher values in the tail of the ratio of induced (local) fields to the upstream IMF for intervals of lower upstream dynamic pressure (Figure 6d), thus following the same trend observed on the dayside. While significant magnetic fields are occasionally present in the tail, these also generally occur in concert with larger IMF fields, as are observed also on the dayside. Separating the solar wind dynamic pressure into its components, we notice that there is little evidence for systematic variation in the values of this ratio with increasing solar wind speed seen by comparing Figures 6g–6i. However, the equivalent grouping by solar wind density shown in Figures 6j, 6k and 6l resemble the patterns seen in the  $P_{\text{dyn}}$  cases (Figures 6d–6f), thus at least tentatively suggesting that the upstream density has a larger controlling influence on the structure of the induced magnetosphere than the solar wind velocity does.

Consideration of conservation of magnetic flux (per unit length through the page) through the region of highlighted IMF field lines in Figure 8, yields the relationship  $|B|_{\text{IM}}/|B|_{\text{IMF}} = X_{\text{Tail}}/X_{\text{IM}}$ , which can be used therefore to estimate the region of the undisturbed solar wind and IMF at large distance from Mars which is magnetically connected to the dayside induced magnetosphere. While the MPB and bow shock have both been shown to move closer to the planet during intervals of high dynamic pressure (e.g., Edberg et al., 2009; Halekas, Brain, et al., 2017; Hall et al., 2016; Hall et al., 2019; Ramstad, Barabash, Futaana, & Holmström, 2017; Matsunaga et al., 2017), the amplitude of this motion is only a small fraction of a Mars radius at the sub-solar point. Assuming that the MPB altitude at the subsolar point corresponds to  $X_{\text{IM}}$  and taking it to be a constant,  $X_{\text{IM}} = 0.3R_M$ , calculated using the Vignes et al. (2000) model,  $X_{\text{Tail}}$  then ranges between  $\sim 8,000$  km ( $\sim 2.4R_M$ ) and  $\sim 13,000$  km ( $\sim 3.7R_M$ ), for high and low  $P_{\text{dyn}}$ , respectively (using the mean ratio shown in Table 2 for the whole dayside). Thus, while the induced magnetosphere and associated plasma boundaries are compressed during intervals of higher upstream pressure, the spatial extent in the solar wind of IMF flux-tubes that thread and form the induced magnetosphere is in fact larger during intervals of lower dynamic pressure. We note that while the relationship expressed above and in Equation 2 was obtained by considering only conservation of flux along the Mars-Sun line, the relatively weak dependence of  $|B|_{\text{IM}}$  on solar zenith angle permits the extrapolation of the calculation to a large fraction of the dayside region. This observation may provide some indication of the mechanisms at work that lead to the observed enhancement in the efficiency of transfer of energy from the solar wind to the escaping ionospheric plasma observed by MEX during intervals of lower dynamic pressure (Ramstad, Barabash, Futaana, Nilsson, & Holmström, 2017), as a relatively larger volume of the solar wind is perturbed in its passage through and around the Martian system. By further dividing  $X_{\text{Tail}}$  with the corresponding mean solar wind speed ( $|v|_{\text{sw}}$ ) for each case, we get also a rough estimate for the timescale solar wind needs to cover the  $X_{\text{Tail}}$  distance and that ranges from  $\sim 18$  to  $\sim 32$  s for high and low  $P_{\text{dyn}}$ , respectively. We note that such short values, statistically determined though they are, indeed are close to the fidelity of our available data, defined by the median spacing between SWIA and MARSIS measurements of  $\sim 16$  s. Moreover, the estimates of this timescale are consistent within a factor of  $\sim 2$  to those obtained by Harada et al. (2017) in tracking a pressure pulse from the solar wind through the induced magnetosphere. We reiterate, however, that such arguments based on these field strength ratios and the conservation of magnetic flux should not be over-interpreted, as they are strictly only applicable in limited circumstances, specifically where the X-component of the IMF is small.

Many details of the electrodynamics of the Martian induced magnetosphere remain poorly understood. The ‘canonical’ picture is one in which enhanced upstream dynamic pressures in particular are responsible for enhanced induced fields (Crider et al., 2003; Girazian et al., 2019), increased atmospheric escape (Girazian et al., 2019; Lundin et al., 2008; Nilsson et al., 2010), and more activity in the tail (Girazian et al., 2019). However, taken together, our results suggest that some caution should be taken in describing such dependencies, since the induced fields themselves are conversely more significantly enhanced relative to the IMF during intervals of lower dynamic pressure.

#### 4. Conclusions

Using magnetic field magnitude measurements from MEX in the induced magnetosphere of Mars and upstream solar wind parameters from MAVEN, we have found that

1. Even though high solar wind dynamic pressure results in stronger induced magnetic fields in the dayside ionosphere, the ratio  $|B|_{\text{IM}}/|B|_{\text{IMF}}$  decreases with increasing solar wind dynamic pressure

2. Comparing the induced fields to the instantaneous IMF, we reveal more of the structure in the vicinity of the MPB, where the reductions in the relative fields above MPB are more evident than in the field strength itself
3. Higher values of the mean  $|B|_{IM}$  are observed in the +E hemisphere, both on the dayside irrespective of latitude and when we restrict northern latitudes only
4. There is a  $\sim 41\%$  increase of the mean  $|B|_{IM}$ , between low and high  $P_{dyn}$  in the dayside
5. There is a  $\sim 36\%$  decrease of the mean ratio  $|B|_{IM}/|B|_{IMF}$  from low to high  $P_{dyn}$  in the dayside
6. The spatial extent in the solar wind of IMF flux-tubes that thread and form the induced magnetosphere is larger during intervals of lower dynamic pressure and we estimate that  $X_{Tail}$  ranges from  $\sim 8,000$  km ( $\sim 2.4R_M$ ) to  $\sim 13,000$  km ( $\sim 3.7R_M$ ), for high and low  $P_{dyn}$ , respectively

Further investigation is needed for a comprehensive description of the induced magnetosphere's response to various parameters, in particular through studying the system's response to immediate upstream conditions in a more complete approach than can be achieved using only field magnitudes estimated by MARSIS. Other external drivers, such as seasonal and solar-cycle driven variations in ionospheric density due to changing ionizing flux were briefly investigated in this analysis but reliable conclusions could not be drawn given the need to first account for the larger observed dependencies on upstream conditions in the solar wind. Future studies utilizing solar wind data from other sources are necessary to fully explore all controlling factors, and further investigate spatial variations that may be associated for example, with the location of Mars' strongest regions of crustal magnetic fields and diurnal asymmetries.

## Data Availability Statement

All the raw MEX and MAVEN data used in this study are available at the NASA Planetary Data System (<https://pds-ppi.igpp.ucla.edu/search/?sc=Mars%20Express&t=Mars&i=MARSIS>), (<https://pds-ppi.igpp.ucla.edu/search/view/?f=yes&id=pds://PPI/maven.mag.calibrated>), (<https://pds-ppi.igpp.ucla.edu/search/view/?f=yes&id=pds://PPI/maven.swia.calibrated>). The MEX data are also available via the ESA Planetary Science Archive (<https://archives.esac.esa.int/>). The production of higher level derived products is detailed in the text.

## Acknowledgments

K. S. and D. J. A. acknowledge support from the Swedish National Space Agency through Grants DNR 156/16 and 162/14. M. L. and B. S.-C. acknowledge support from UK-STFC Grant ST/S000429/1. B.S.-C. also acknowledges support through STFC Ernest Rutherford Fellowship ST/V004115/1.

## References

- Akalın, F., Morgan, D. D., Gurnett, D. A., Kirchner, D. L., Brain, D. A., Modolo, R., et al. (2010). Dayside induced magnetic field in the ionosphere of Mars. *Icarus*, 206(1), 104–111. <https://doi.org/10.1016/j.icarus.2009.03.021>
- Andrews, D. J., Edberg, N. J. T., Eriksson, A. I., Gurnett, D. A., Morgan, D., Němec, F., & Opgenoorth, H. J. (2015). Control of the topside Martian ionosphere by crustal magnetic fields. *Journal of Geophysical Research: Space Physics*, 120, 3042–3058. <https://doi.org/10.1002/2014JA020703>
- Andrews, D. J., Opgenoorth, H. J., Edberg, N. J., André, M., Fränz, M., Dubinin, E., et al. (2013). Determination of local plasma densities with the MARSIS radar: Asymmetries in the high-altitude Martian ionosphere. *Journal of Geophysical Research: Space Physics*, 118, 6188–6242. <https://doi.org/10.1002/jgra.50593>
- Bertucci, C., Duru, F., Edberg, N., Fraenz, M., Martinez, C., Szego, K., & Vaisberg, O. (2011). The induced magnetospheres of Mars, Venus, and Titan. *Space Science Reviews*, 162, 113–171. <https://doi.org/10.1007/s11214-011-9845-1>
- Bonett, G. D., & Wright, A. T. (2000). Sample size requirements for estimating Pearson, Kendall and Spearman correlations. *Psychometrika*, 65(1), 23–28. <https://doi.org/10.1007/bf02294183>
- Brain, D. A., Halekas, J. S., Lillis, R., Mitchell, D. L., Lin, R. P., & Crider, D. H. (2005). Variability of the altitude of the Martian sheath. *Geophysical Research Letters*, 32(18), 1–4. <https://doi.org/10.1029/2005GL023126>
- Cain, J. C., Ferguson, B. B., & Mozzoni, D. (2003). An  $n = 90$  internal potential function of the Martian crustal magnetic field. *Journal of Geophysical Research*, 108, 5008. <https://doi.org/10.1029/2000je001487>
- Connerney, J. E., Espley, J., Lawton, P., Murphy, S., Odom, J., Oliverson, R., & Sheppard, D. (2015). The MAVEN magnetic field investigation. *Space Science Reviews*, 195, 257–291. <https://doi.org/10.1007/s11214-015-0169-4>
- Crider, D. H., Vignes, D., Krymskii, A. M., Breus, T. K., Ness, N. F., Mitchell, D. L., et al. (2003). A proxy for determining solar wind dynamic pressure at Mars using Mars Global Surveyor data. *Journal of Geophysical Research: Space Physics*, 108(A12), 1–10. <https://doi.org/10.1029/2003JA009875>
- DiBraccio, G. A., Luhmann, J. G., Curry, S. M., Espley, J. R., Xu, S., Mitchell, D. L., et al. (2018). The twisted configuration of the martian magnetotail: MAVEN observations. *Geophysical Research Letters*, 45(10), 4559–4568. <https://doi.org/10.1029/2018GL077251>
- Dong, Y., Fang, X., Brain, D. A., McFadden, J. P., Halekas, J. S., Connerney, J. E., et al. (2015). Strong plume fluxes at Mars observed by MAVEN: An important planetary ion escape channel. *Geophysical Research Letters*, 42(21), 8942–8950. <https://doi.org/10.1002/2015GL065346>
- Dubinin, E., Modolo, R., Fraenz, M., Pätzold, M., Woch, J., Chai, L., et al. (2019). The induced magnetosphere of Mars: Asymmetrical topology of the magnetic field lines. *Geophysical Research Letters*, 46(22), 12722–12730. <https://doi.org/10.1029/2019GL084387>
- Dubinin, E., Modolo, R., Fraenz, M., Woch, J., Duru, F., Akalın, F., et al. (2008). Structure and dynamics of the solar wind/ionosphere interface on Mars: MEX-ASPERA-3 and MEX-MARSIS observations. *Geophysical Research Letters*, 35(11), 2–7. <https://doi.org/10.1029/2008GL033730>

- Duru, F., Gurnett, D. A., Frahm, R. A., Winningham, J. D., Morgan, D. D., & Howes, G. G. (2009). Steep, transient density gradients in the Martian ionosphere similar to the ionopause at Venus. *Journal of Geophysical Research: Space Physics*, 114, 1–17. <https://doi.org/10.1029/2009JA014711>
- Duru, F., Gurnett, D. A., Morgan, D. D., Modolo, R., Nagy, A. F., & Najib, D. (2008). Electron densities in the upper ionosphere of Mars from the excitation of electron plasma oscillations. *Journal of Geophysical Research: Space Physics*, 113, A07302. <https://doi.org/10.1029/2008JA013073>
- Edberg, N. J. T., Brain, D. A., Lester, M., Cowley, S. W., Modolo, R., Fränz, M., & Barabash, S. (2009). Plasma boundary variability at Mars as observed by Mars global surveyor and Mars express. *Annales Geophysicae*, 27, 3537–3550. <https://doi.org/10.5194/angeo-27-3537-2009>
- Edberg, N. J. T., Lester, M., Cowley, S. W., & Eriksson, A. I. (2008). Statistical analysis of the location of the Martian magnetic pileup boundary and bow shock and the influence of crustal magnetic fields. *Journal of Geophysical Research: Space Physics*, 113, 1–8. <https://doi.org/10.1029/2008JA013096>
- Fillingim, M. O., Lillis, R. J., England, S. L., Peticolas, L. M., Brain, D. A., Halekas, J. S., et al. (2012). On wind-driven electrojets at magnetic cusps in the nightside ionosphere of Mars. *Earth Planets and Space*, 64(2), 93–103. <https://doi.org/10.5047/eps.2011.04.010>
- Fisher, R. A. (1921). On the probable error of a coefficient of correlation deduced from a small sample. *Metron*, (1), 3–32. <https://hdl.handle.net/2440/15169>
- Girazian, Z., Halekas, J., Morgan, D. D., Kopf, A. J., Gurnett, D. A., & Chu, F. (2019). The effects of solar wind dynamic pressure on the structure of the topside ionosphere of Mars. *Geophysical Research Letters*, 46(15), 8652–8662. <https://doi.org/10.1029/2019gl083643>
- Gruesbeck, J. R., Espley, J. R., Connerney, J. E., DiBraccio, G. A., Soobiah, Y. I., Brain, D., et al. (2018). The three-dimensional bow shock of Mars as observed by MAVEN. *Journal of Geophysical Research: Space Physics*, 123(6), 4542–4555. <https://doi.org/10.1029/2018JA025366>
- Gurnett, D. A., Kirchner, D. L., Huff, R. L., Morgan, D. D., Persoon, A. M., Averkamp, T. F., et al. (2005). Radar soundings of the ionosphere of Mars. *Science*, 310, 1929–1933. <https://doi.org/10.1126/science.1121868>
- Halekas, J. S., Brain, D. A., Luhmann, J. G., DiBraccio, G. A., Ruhunusiri, S., Harada, Y., et al. (2017). Flows, fields, and Forces in the Mars-solar wind interaction. *Journal of Geophysical Research: Space Physics*, 122(11), 11320–11342. <https://doi.org/10.1002/2017JA024772>
- Halekas, J. S., McFadden, J. P., Brain, D. A., Luhmann, J. G., DiBraccio, G. A., Connerney, J. E., et al. (2018). Structure and variability of the martian ion composition boundary layer. *Journal of Geophysical Research: Space Physics*, 123(10), 8439–8458. <https://doi.org/10.1029/2018JA025866>
- Halekas, J. S., Ruhunusiri, S., Harada, Y., Collinson, G., Mitchell, D. L., Mazelle, C., et al. (2017). Structure, dynamics, and seasonal variability of the Mars-solar wind interaction: MAVEN solar wind ion analyzer in-flight performance and science results. *Journal of Geophysical Research: Space Physics*, 122, 547–578. <https://doi.org/10.1002/2016JA023167>
- Halekas, J. S., Taylor, E. R., Dalton, G., Johnson, G., Curtis, D. W., McFadden, J. P., et al. (2015). The solar wind ion analyzer for MAVEN. *Space Science Reviews*, 195, 125–151. <https://doi.org/10.1007/s1214-013-0029-z>
- Hall, B. E., Lester, M., Sánchez-Cano, B., Nichols, J. D., Andrews, D. J., Edberg, N. J., et al. (2016). Annual variations in the Martian bow shock location as observed by the Mars Express mission. *Journal of Geophysical Research: Space Physics*, 121(11), 11474–11494. <https://doi.org/10.1002/2016JA023316>
- Hall, B. E., Sánchez-Cano, B., Wild, J. A., Lester, M., & Holmström, M. (2019). The martian bow shock over solar cycle 23–24 as observed by the Mars express mission. *Journal of Geophysical Research: Space Physics*, 124(6), 4761–4772. <https://doi.org/10.1029/2018JA026404>
- Harada, Y., Gurnett, D. A., Kopf, A. J., Halekas, J. S., Ruhunusiri, S., Lee, C. O., et al. (2017). Dynamic response of the martian ionosphere to an interplanetary shock: Mars express and MAVEN observations. *Geophysical Research Letters*, 44, 9116–9123. <https://doi.org/10.1002/2017GL074897>
- Holmberg, M. K., André, N., Garnier, P., Modolo, R., Andersson, L., Halekas, J., et al. (2019). MAVEN and MEX multi-instrument study of the dayside of the martian induced magnetospheric structure revealed by pressure analyses. *Journal of Geophysical Research: Space Physics*, 124(11), 8564–8589. <https://doi.org/10.1029/2019JA026954>
- Jordan, R., Picardi, G., Plaut, J., Wheeler, K., Kirchner, D., Safaeinili, A., et al. (2009). The Mars express MARSIS sounder instrument. *Planetary and Space Science*, 57, 1975–1986. <https://doi.org/10.1016/j.pss.2009.09.016>
- Luhmann, J. G., & Cravens, T. (1991). Magnetic fields in the ionosphere of Venus. *Space Science Reviews*, 55, 201–274. [https://doi.org/10.1007/978-94-011-3300-5\\_4](https://doi.org/10.1007/978-94-011-3300-5_4)
- Lundin, R., Barabash, S., Fedorov, A., Holmström, M., Nilsson, H., Sauvaud, J. A., & Yamuchi, M. (2008). Solar forcing and planetary ion escape from Mars. *Geophysical Research Letters*, 35(9), 1–5. <https://doi.org/10.1029/2007GL032884>
- Matsunaga, K., Seki, K., Brain, D. A., Hara, T., Masunaga, K., McFadden, J. P., et al. (2017). Statistical study of Relations between the induced magnetosphere, ion composition, and pressure balance boundaries around Mars based on MAVEN observations. *Journal of Geophysical Research: Space Physics*, 122(9), 9723–9737. <https://doi.org/10.1002/2017JA024217>
- Mazelle, C., Winterhalter, D., Sauer, K., Trotignon, J. G., Acuña, M. H., Baumgärtel, K., et al. (2004). Bow shock and upstream phenomena at Mars. *Space Science Reviews*, 111(1–2), 115–181. <https://doi.org/10.1023/B:SPAC.0000032717.98679.d0>
- Nagy, A. F., Winterhalter, D., Sauer, K., Cravens, T. E., Brecht, S. H., Mazelle, C., et al. (2004). The plasma environment of Mars. *Space Science Reviews*, 111, 33–114. <https://doi.org/10.1023/B:SPAC.0000032718.47512.92>
- Němec, F., Linzmayer, V., Němeček, Z., & Šafránková, J. (2020). Martian bow shock and magnetic pileup boundary models based on an automated region identification. *Journal of Geophysical Research: Space Physics*, 125(11), 1–16. <https://doi.org/10.1029/2020JA028509>
- Nilsson, H., Carlsson, E., Brain, D. A., Yamauchi, M., Holmström, M., Barabash, S., et al. (2010). Ion escape from Mars as a function of solar wind conditions: A statistical study. *Icarus*, 206(1), 40–49. <https://doi.org/10.1016/j.icarus.2009.03.006>
- Picardi, G., Biccari, D., Seu, R., Plaut, J., Johnson, W. T. K., Jordan, R. L., & Zampolini, E. (2004). Marsis : Mars advanced radar for subsurface and ionosphere sounding. In A. Wilson, & A. Chicarro (Eds.), (Vol. 1240, pp. 51–69). ESA Publications Division. Mars express: The scientific payload, esa special publication.
- Ramstad, R., Barabash, S., Futaana, Y., & Holmström, M. (2017). Solar wind- and EUV-dependent models for the shapes of the Martian plasma boundaries based on Mars Express measurements. *Journal of Geophysical Research: Space Physics*, 122(7), 7279–7290. <https://doi.org/10.1002/2017JA024098>
- Ramstad, R., Barabash, S., Futaana, Y., Nilsson, H., & Holmström, M. (2017). Global Mars-solar wind coupling and ion escape. *Journal of Geophysical Research: Space Physics*, 122(8), 8051–8062. <https://doi.org/10.1002/2017JA024306>
- Ramstad, R., Brain, D. A., Dong, Y., Espley, J., Halekas, J., & Jakosky, B. (2020). The global current systems of the Martian induced magnetosphere. *Nature Astronomy*, 4(10), 979–985. <https://doi.org/10.1038/s41550-020-1099-y>
- Russell, C. T., Luhmann, J. G., & Strangeway, R. J. (2016). *Space Physics*. Cambridge University Press.
- Sánchez-Cano, B., Narvaez, C., Lester, M., Mendillo, M., Mayyasi, M., Holmstrom, M., et al. (2020). Mars' ionopause: A matter of pressures. *Journal of Geophysical Research: Space Physics*, 125, e2020JA028145. <https://doi.org/10.1029/2020JA028145>

- Trotignon, J. G., Mazelle, C., Bertucci, C., & Acuña, M. H. (2006). Martian shock and magnetic pile-up boundary positions and shapes determined from the Phobos 2 and Mars Global Surveyor data sets. *Planetary and Space Science*, 54, 357–369. <https://doi.org/10.1016/j.pss.2006.01.003>
- Vignes, D., Mazelle, C., Rme, H., Acuña, M. H., Connerney, J. E., Lin, R. P., et al. (2000). The solar wind interaction with Mars: Locations and shapes of the bow shock and the magnetic pile-up boundary from the observations of the MAG/ER experiment onboard Mars global surveyor. *Geophysical Research Letters*, 27, 49–52. <https://doi.org/10.1029/1999GL010703>
- Wang, M., Lee, L. C., Xie, L., Xu, X., Lu, J. Y., Kabin, K., et al. (2021). Effect of solar wind density and velocity on the subsolar standoff distance of the Martian magnetic pileup boundary. *Astronomy & Astrophysics*, 651(A22), A22. <https://doi.org/10.1051/0004-6361/202140511>
- Wang, M., Xie, L., Lee, L. C., Xu, X. J., Kabin, K., Lu, J. Y., et al. (2020). A 3D parametric martian bow shock model with the effects of mach number, dynamic pressure, and the interplanetary magnetic field. *The Astrophysical Journal*, 903(2), 125. <https://doi.org/10.3847/1538-4357/abbc04>
- Withers, P., Mendillo, M., Rishbeth, H., Hinson, D. P., & Arkani-Hamed, J. (2005). Ionospheric characteristics above Martian crustal magnetic anomalies. *Geophysical Research Letters*, 32(16), 1–4. <https://doi.org/10.1029/2005GL023483>
- Xu, S., Mitchell, D. L., Weber, T., Brain, D. A., Luhmann, J. G., Dong, C., et al. (2020). Characterizing Mars's magnetotail topology with respect to the upstream interplanetary magnetic fields. *Journal of Geophysical Research: Space Physics*, 125(3), e2019JA027755. <https://doi.org/10.1029/2019JA027755>